Enabling High-Frequency Operation of MMC-Based Chargers: Frequency-Decoupled Modulation Strategy and Soft Switching

Kaveh Pouresmaeil, *Graduate Student Member, IEEE*, Maurice G. L. Roes, *Member, IEEE*, Nico H. Baars, and George A. Papafotiou, *Member, IEEE*

***Abstract*—The demand for ultrafast charging of electric heavy-duty vehicles drives the development of megawatt-level interfaces with the medium-voltage grid. Modular multilevel converter (MMC)-based chargers offer a promising solution, utilizing a single medium-frequency transformer (MFT) to enhance power density. This article proposes a novel modulation strategy for ac/ac MMCs with rectangular-wave output that leverages the separation of low-frequency and medium-frequency components within the modulation stage. This separation reduces the scaling factor between the switching frequency and the MFT's operating frequency, enabling the use of higher operating frequencies for the MFT. This, in turn, facilitates the size reduction of the MFT without compromising the efficiency of the MMC. The findings demonstrate significant improvements in the modulator, including higher time resolution of waveform synthesis, and reduced harmonic distortion in the MMC's terminal voltages and currents. This, in turn, enables soft-switching operation in the power converters. Experimental results are given to validate the theoretical analysis and practical feasibility of the proposed modulation and soft-switching strategies.**

***Index Terms*—AC/AC converters, AC/DC converter, charging infrastructures, modular multilevel converters (MMCs), modulation, soft-switching, transformer.**

I. Introduction

MODULAR multilevel converters (MMCs) have gained significant traction in medium-voltage (MV) high-power applications due to modularity, scalability, and low harmonic distortion. Their capability for direct ac/ac conversion enables integration of a medium-frequency (MF) isolation stage, making them a compact solution for isolated applications, such as ultrafast chargers. These chargers process megawatt (MW)-level power and, therefore, require connection to the MV grid. Conventional solutions apply a low-frequency (LF) transformer or several medium-frequency transformer (MFTs) (in multicell solutions) to provide the galvanic isolation and the voltage matching. The LF transformer is bulky and multicell solutions (e.g., cascaded H-bridge) require isolation levels selected based on the MV grid voltage for all the MFTs [1], [2]. In this regard, solutions based on a single MFT can be more appealing for size/volume constrained applications. Kopacz et al. [3] proposed a matrix-type ac/ac MMC converter integrating a single three-phase MFT. Although matrix-type converters require the minimum number of semiconductors and the least internal energy storage effort compared to other solutions, they introduce higher control complexity and cannot fully decouple the LF and MF terminal variables [4], [5], which can, in turn, complicate the design of the MFT. On the other hand, the direct ac/ac MMC architecture can reduce the system size and cost by using a single MFT and provides complete decoupling between the LF and MF terminal variables [6], [7]. Fig. 1 illustrates the architecture of an ac/ac-MMC-based ultrafast charger. Here, the MMC operates as an ac/ac converter, transforming the grid voltage into a MF ac voltage. Various waveforms can be chosen as the MMC's output waveform, but rectangular voltage has been shown to result in the optimum efficiency and pulsating power [7], [8], [9], [10]. Another rectangular voltage is generated by the low-voltage converter (LVC) that switches with a 50% duty cycle. These voltage sources, interconnected by means of the arm inductors and the MFT, govern the power transfer between the MMC and the LVC.

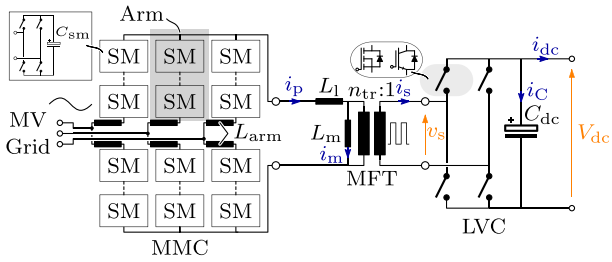

Fig. 1. Circuit configuration of an AC/AC-MMC-based ultrafast charger.

For an MW-level MFT, existing literature demonstrates the feasibility of operating at frequencies around 5 kHz [11]. However, this frequency selection is constrained here by the permissible power losses of the converter connected to the transformer. Theoretical studies show the optimal power density is achieved

Received 5 August 2024; revised 1 November 2024 and 17 December 2024; accepted 10 January 2025. Date of publication 27 January 2025; date of current version 20 March 2025. This work was supported by the NEON under Grant 17628 of the research programme Crossover which is supported in part by the Dutch Research Council (NWO). Recommended for publication by Associate Editor Q. Wei. *(Corresponding author: Kaveh Pouresmaeil.)*

The authors are with the Department of Electrical Engineering, Eindhoven University of Technology, 5600MB Eindhoven, The Netherlands (e-mail: k.pouresmaeil@tue.nl).

Color versions of one or more figures in this article are available at https://doi.org/10.1109/TPEL.2025.3534427.

Digital Object Identifier 10.1109/TPEL.2025.3534427

when operating within 7–10 kHz [12]. Moreover, operating the MFT at 10 kHz shifts acoustic noise out of the audible range, as magnetostriction noise occurs at twice the operating frequency. However, for the ac/ac MMC, the transformer's operating frequency is limited to a few hundred hertz or, at maximum, a few kilohertz (e.g., 1–2 kHz) due to efficiency constraints [13], [14], [15]. The limitation of the operating frequency of the MFT directly impacts its performance optimization. This limitation stems from the fact that the high operating frequency of the isolation stage implies a high switching frequency of the power devices. The MMC is an interface between its three-phase input and single-phase output terminals. Consequently, the reference for the MMC's arm voltages requires components at both LF (sine-wave voltage) and MF (rectangular-wave voltage). The most common technique for synthesizing these voltage references is through carrier-based pulse width modulation (CB-PWM), where the modulation index of the arm is compared with several carrier waveforms [16], [17]. The harmonic distortion of the input and output terminal' currents is a function of the MMC's arm voltage distortion. To minimize harmonic distortion in the synthesized voltage waveforms, the carrier frequency must be significantly higher than the highest frequency present in the reference signal (i.e., the MF component) [18]. Increased carrier frequency translates to a higher switching frequency per device in the MMC. This is easily manageable for ac/dc MMCs, as the highest frequency present in the arm voltage is the grid frequency. However, it necessitates a very high carrier frequency for the ac/ac MMC. Another challenge results from the PWM update rate in digital control; the modulation index of each MMC arm is typically sampled only once or twice per modulation period. This limited time resolution restricts the accuracy of the generated voltage components, particularly the MF rectangular component used for the MFT [7]. As a result, these methods require a high carrier frequency (or, equivalently, a high switching frequency) to generate a rectangular voltage with low distortion and high time resolution in the MMC's arm.

This article proposes a frequency-decoupled (FD) modulation strategy for the ac/ac MMC with an MF rectangular-wave output. This modulation method enables independent selection of the modulation strategy and its parameters for both frequency (LF and MF) components of the arm voltage. Therefore, the CB-PWM and nearest level modulation (NLM) are adapted to synthesis the LF and MF components of the arm voltage, respectively. This combination allows for a low carrier frequency of CB-PWM, resulting in a low switching frequency, while increasing the operating frequency of the transformer. The authors in [19] and [20] introduced and applied the decoupled modulation concept to an ac/ac MMC for railway supplies with a single-phase 16.7 Hz sine-wave output and identified phase-shifted CB-PWM as the best modulation method for the single-phase side output. While CB-PWM is preferred for sine-wave operation due to its superior harmonic performance for a single-frequency reference signal, it is not designed to synthesize a rectangular-wave modulation signal and therefore requires a very high carrier frequency (on the order of several hundred kilohertz) if applied in this context.

In addition, soft switching techniques can facilitate high-frequency operation in power converters [21]. However, due to the mix of MF and LF components in the arm voltage and current, the MMC is typically hard-switched, which further limits the switching frequency of the power devices and in turn the output frequency of the MMC [22]. Dijkhuizen et al. [23] achieved soft-switching operation in the MMC using an auxiliary resonant commutated pole converter. However, this adds to the system's cost and complexity. Fuchs et al. [33] proposed a concept for a single-phase to single-phase ac/ac MMC in which the rectangular voltages generated by the MMC and the LVC make the MMC operation equivalent to a dual active bridge (DAB) converter. However, this study only presents the theoretical concept without discussing the switching events in detail. In that regard, the key contributions of this article are as follows.

1) An FD modulation strategy for ac/ac MMC with MF rectangular-wave output is proposed and analyzed. This strategy utilizes CB-PWM and NLM for synthesizing the LF and MF componenets of the arm voltages, respectively. Compared to conventional methods [20], it offers significantly improved harmonic performance and time resolution for elevated operating frequencies of the MFT.
2) Utilizing the low-distortion MF current, DAB-like operation mode is obtained for three-phase to single-phase ac/ac MMC. This approach enables zero-voltage switching (ZVS) not only for all switching events in the LVC but also for those related to the MF component in the MMC, provided suitable circuit parameters are selected.

The rest of this article is organized as follows. The system model and operating principle are presented in Section II. Section III compares the conventional and proposed modulation methods on the basis of voltage waveform distortion and resolution. The soft-switching operation and the control scheme are presented in Sections IV and V, respectively. Simulation and experimental results are provided in Sections VI and VII, respectively. Finally, Section VIII concludes this article.

II. System Model

In the MMC, each arm consists of a series connection of several submodules, whose ac-link voltages are a function of their dc-link voltages and switching functions. Hence, each submodule, and therefore the aggregate of all submodules in one arm of the MMC can be modeled by a controlled voltage source, as shown in Fig. 2. The arm voltages $v_{\mathrm{y}}^{\mathrm{x}}$ ($\mathrm{y} \in \{\mathrm{a},\mathrm{b},\mathrm{c}\}$, $\mathrm{x} \in \{\mathrm{u},\mathrm{l}\}$) are composed of differential-mode and common-mode components. Common-mode (Σ) and differential-mode (Δ) components of the arm voltages and currents can be defined as

$$\begin{cases} v_{\mathrm{y}}^{\Sigma} = \frac{v_{\mathrm{y}}^{\mathrm{u}} + v_{\mathrm{y}}^{\mathrm{l}}}{2} \\ i_{\mathrm{y}}^{\Sigma} = \frac{i_{\mathrm{y}}^{\mathrm{u}} + i_{\mathrm{y}}^{\mathrm{l}}}{2} \\ v_{\mathrm{y}}^{\Delta} = \frac{v_{\mathrm{y}}^{\mathrm{u}} - v_{\mathrm{y}}^{\mathrm{l}}}{2} \\ i_{\mathrm{y}}^{\Delta} = \frac{i_{\mathrm{y}}^{\mathrm{u}} - i_{\mathrm{y}}^{\mathrm{l}}}{2}. \end{cases}, \text{where}\, \mathrm{y} \in \{\mathrm{a},\mathrm{b},\mathrm{c}\} \tag{1}$$

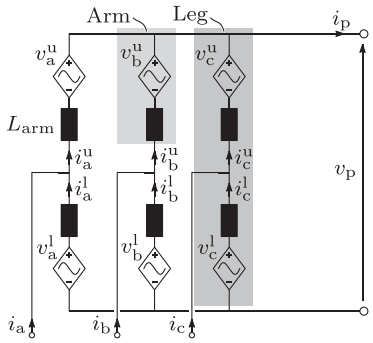

Fig. 2. Equivalent circuit of the AC/AC MMC.

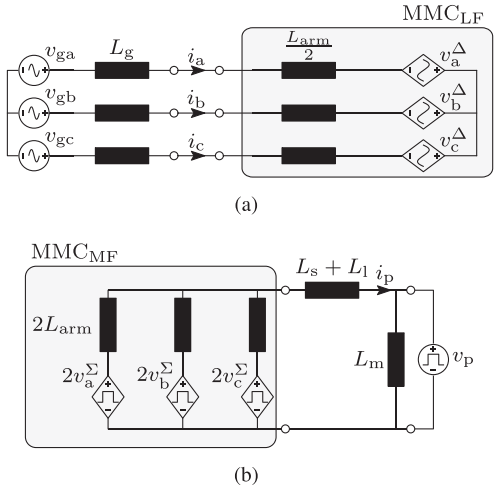

Fig. 3. (a) LF-terminal model of the MMC. (b) MF-terminal model of the MMC.

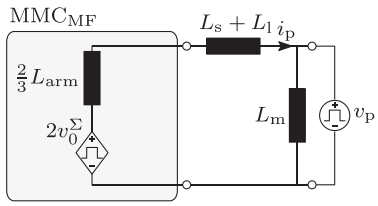

Fig. 4. Rearranged MF terminal model.

Analyzing the leg current and voltage components illustrates that the MMC and LV grid interact through the differential-mode components. On the other hand, the interaction between the MMC and MF side is governed by the common-mode components [9], [16]. As a result, two decoupled models can be defined for the MMC, as shown in Fig. 3. Under balanced circuit parameters, the circulating terms are zero in steady-sate and are not present in the arm common-mode voltage v_y^Σ [8]. Hence, the MF terminal model of the MMC, shown in Fig. 3(b), can be rearranged using Thevenin's theorem, as depicted in Fig. 4. In the rearranged MF terminal model, the voltage $2v_0^\Sigma$ is equivalent to the MMC's output common-mode voltage, which can be used to control the active and reactive power exchange between the MMC and the LVC. As a result, the MF-terminal model of the MMC can be interpreted as a DAB converter. The transferred power and its direction can be adjusted by changing the phase shift φ_{MF} between the rectangular voltage $2v_0^\Sigma$ and v_p. Similar

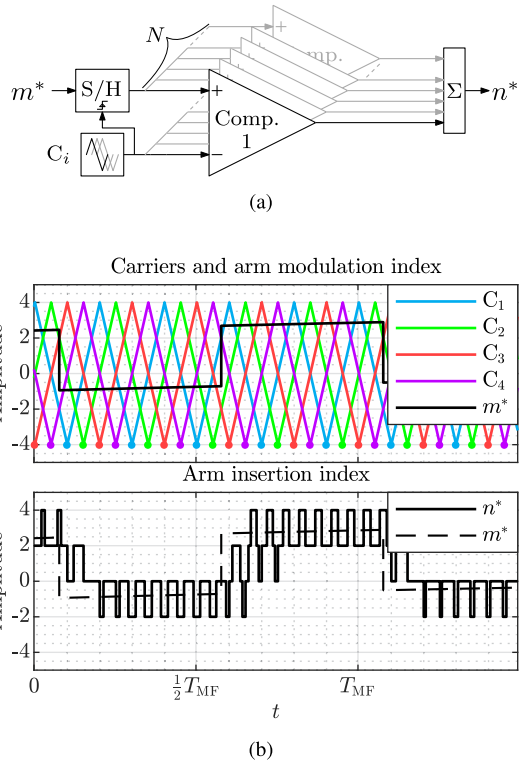

Fig. 5. (a) Diagram of PSC-PWM and (b) simulated waveform of an MMC arm with four submodules operating with PSC-PWM; "•" represents the update of the modulation index for each carrier waveform (the PWM update rate is assumed to be single rate).

to a typical DAB converter [24], the transferred average power can be derived as

$$P = \frac{2V_0^\Sigma V_p}{2\pi f_{MF} L} \frac{\varphi_{MF}}{\pi} \left(\pi - |\varphi_{MF}|\right), \tag{2}$$

$$\text{where} \begin{cases} V_p = n_{tr} V_{dc} \\ L = \frac{2}{3} L_{arm} + L_s + L_l. \end{cases}$$

III. Modulation Strategy of the MMC

The reference voltage and similarly the modulation index of the arm are constructed by summing up LF and MF reference components. Therefore, the reference modulation index, m^* is obtained by

$$m^* = m^*_{LF} + m^*_{MF}. \tag{3}$$

A. Conventional Modulation Strategies

1) Phase-Shifted Carrier (PSC) Modulation: Using PSC modulation, the modulation index of the arm m^* is first sampled with single or double update-rate and then compared to the carrier signals C_i, ranging from $-N$ to N and shifted in phase by 2π N, to generate the insertion index n^* of the arm. The equivalent carrier frequency of the arm and switching frequency per device are equal to $f_{c,eq} = N f_c$ and $f_{d,sw} = f_c$, respectively, since all the submodules switch in one carrier period as seen in Fig. 5. Fig. 5(b) illustrates the staircase-like behavior of CB-PWM. Due to this behavior, the generated insertion index of the arm and therefore voltage waveform present a slew rate.

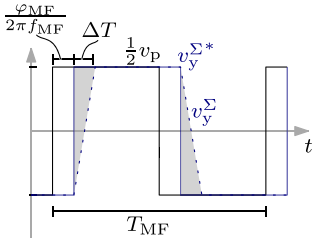

Fig. 6. Theoretical reference and generated common-mode arm voltages.

This slew rate can cause a time delay of $\frac{1}{f_c} = T_c$ in between the reference common-mode arm voltage $v_y^{\Sigma *}$ and the generated voltage v_y^{Σ}, as shown in Fig. 6. This time delay can deteriorate the generated MF voltage waveform and cause an undesired phase shift. This effect can be comparable to the phase angle generated by the closed-loop control of the MMC. This, in turn, limits the accuracy of the control action of energy controllers within the MMC. To ease these issues, the time delay must be kept as short as possible (e.g., $\Delta T \leq 0.01 T_{MF}$). By doing so and assuming single-update rate, the minimum carrier frequency is obtained by

$$f_c \geq 100 f_{MF} \tag{4}$$

which can lead to a very high switching frequency and, therefore, to significant switching losses in the MMC.

2) Level-Shifted Carrier (LSC) Modulation: With LSC modulation, $2N$ carriers are divided over the range from $-N$ to N as shown in Fig. 7. The sampled modulation index of the arm is compared with these carriers and generates the insertion index of the arm. The equivalent carrier frequency of the arm is equal to $f_{c,eq} = f_c$. The switching frequency per device is found to be

$$f_{d,sw} = \frac{1}{N}\left(\lfloor \hat{n}^*_{LF} \rfloor f_g + 0.5 f_c + \hat{n}^*_{MF} f_{MF}\right) \tag{5}$$

with the number of submodules, $\hat{n}^*_{MF} = N^*_{MF}$, which are specifically switching to synthesize the MF component of the arm voltage. Since more than one submodule can switch simultaneously, there is no longer a slew rate in the generated arm voltage. However, the time resolution of the generated waveform is limited by the carrier period, since the modulation signal can be updated once or maximum twice within the carrier period. In order to minimize the time delay (for instance, $\Delta T \leq 0.01 T_{MF}$) and assuming a single update rate, the lowest possible carrier frequency must be selected according to (4).

B. Proposed Modulation Strategy

This section presents frequency-decoupled PWM (FD-PWM) for the ac/ac MMC. As can be seen from Fig. 8(a), the proposed strategy separates the reference modulation index, m^*, into two components: an LF component, m^*_{LF}, and an MF component, m^*_{MF}. Conventionally, the modulation index, m^*, which incorporates both differential and common-mode information, is used for insertion index generation. In the proposed strategy, a decoupled approach is adapted. The LF component, m^*_{LF}, is directly fed to a CB-PWM comparator to generate the LF insertion index, n^*_{LF}. On the other hand, the NLM approach [25] is used to

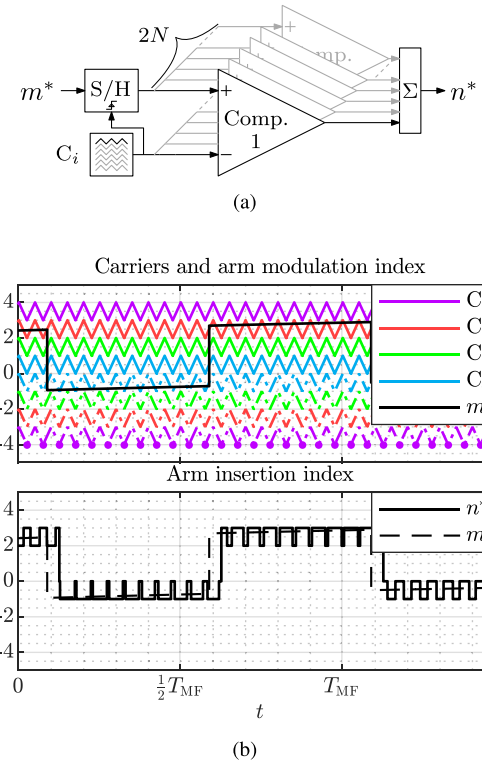

Fig. 7. (a) Diagram of LSC-PWM and (b) simulated waveform of an MMC arm with four submodules operating with LSC modulation; "•" represents the update of the modulation index for each carrier waveform (single-update rate is assumed).

derive the MF insertion index, n^*_{MF}. Here, a triangular carrier waveform, C_{MF}, with a frequency and phase equal to the MF component and ranging from -1 to 1 is employed. This carrier is compared with a zero reference to obtain the normalized MF component, $n^*_{MF,norm}$. The MF insertion index is then calculated by multiplying the normalized MF component with the number of submodules, N^*_{MF}, dedicated to the MF component

$$n^*_{MF} = n^*_{MF,norm} \cdot N^*_{MF}. \tag{6}$$

Here, N^*_{MF} is a discrete number determined by the nearest integer of submodules required to switch and generate the MF component of the arm. The MF insertion index n^*_{MF} is added to the LF insertion index n^*_{LF} to derive the total insertion index n^* of the arm. Compared to LSC-PWM [see Fig. 7(b)], the proposed method exhibits two key improvements, as shown in Fig. 8(b). First, the insertion index pulse train follows a sinusoidal pattern, eliminating the intermodulation effect observed in LSC-PWM (detailed in the following section). Second, the time delay between the reference and generated MF arm voltage is significantly reduced. While LSC-PWM's time resolution is limited by the carrier period, the proposed method's resolution is determined by the high-speed clock generating C_{MF} in a counter implementation, typically in the order of a few nanoseconds.

The switching frequency per device follows the same (5) as that of the LSC-PWM. However, the operating frequency of the transformer can be increased independent of f_c, which enables high frequency operation with a much smaller increase of the

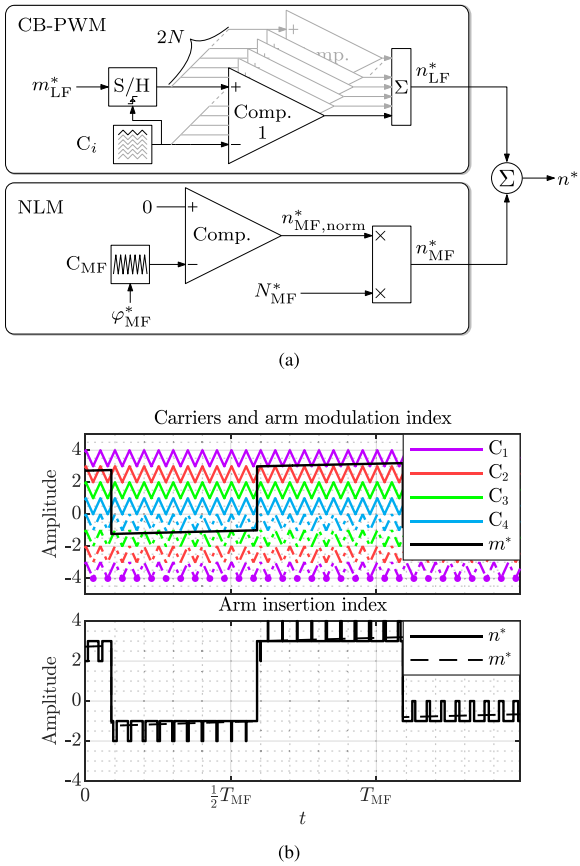

Fig. 8. (a) Diagram of FD-PWM and (b) simulated waveform of an MMC arm with four submodules operating with proposed modulation; "•" represents the update of the modulation index for each carrier waveform (single-update rate is assumed).

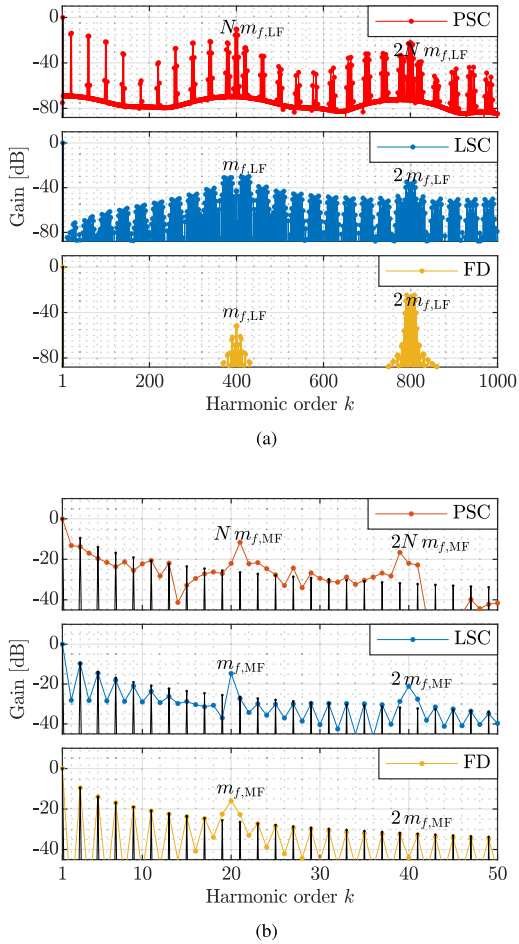

Fig. 9. Theoretical harmonic spectra for different modulation methods (the harmonic spectra of the reference signal is plotted with black line and marker). With $m_{\mathrm{LF}} = m_{\mathrm{MF}} = 1.7$ for PSC-PWM and LSC-PWM and $m_{\mathrm{LF}} = 1.7, N_{\mathrm{MF}} = 2$ for FD-PWM. (a) Magnitude spectra of the LF component of the arm voltage over harmonic number k (the values are normalized based on the fundamental component f_{LF}). (b) Magnitude spectra of the MF component of the arm voltage over harmonic number k (the values are normalized based on the fundamental component f_{MF}).

switching frequency of the power devices in the MMC compared to PSC- and LSC-PWM. Hereafter in this article, LSC-PWM and PSC-PWM will refer to the conventional coupled carrier-based PWM methods, as detailed in Section III-A.

C. Harmonic Performance Comparison

In the previous sections, it is shown that both the PSC- and LSC-PWM methods are associated with limited time resolution when synthesizing the MF component of the arm voltage. In addition to that, the generated voltages are not perfect sinusoidal or rectangular voltages and contain harmonic components. The harmonic performance of these methods is studied in this section. The most common forms of PSC- and LSC-PWM, which does not apply a phase displacement in between the carrier waveforms of the upper and lower arms, are used [26]. Fig. 9(a) and (b) presents the harmonic spectra of the LF component (v_{y}^{Δ}) and MF component (v_{y}^{Σ}) of the of the arm voltage for all the three methods, respectively. The frequency modulation ratio for the LF and MF components are defined as

$$\begin{cases} m_{f,\mathrm{LF}} = \frac{f_{\mathrm{c}}}{f_{\mathrm{LF}}} \\ m_{f,\mathrm{MF}} = \frac{f_{\mathrm{c}}}{f_{\mathrm{MF}}} \end{cases} \tag{7}$$

TABLE I
PWM METHODS AND FREQUENCY MODULATION RATIOS

Frequency modulation ratio	PSC-PWM	LSC-PWM	FD-PWM
$m_{f,\mathrm{LF}}$	100	400	400
$m_{f,\mathrm{MF}}$	5	20	20

which are given in Table I. As shown in Fig. 9(a), for the PSC- and LSC-PWM methods, the modulation index of the arm is modulated by the equivalent carrier frequency of the arm, $f_{\mathrm{c,eq}}$, resulting in sideband harmonics at orders of

$$\begin{cases} hNm_{f,\mathrm{LF}} \pm (2j+1)\frac{m_{f,\mathrm{LF}}}{m_{f,\mathrm{MF}}} \pm (2l+1) & \mathrm{PSC} \\ hm_{f,\mathrm{LF}} \pm (2j+1)\frac{m_{f,\mathrm{LF}}}{m_{f,\mathrm{MF}}} \pm (2l+1) & \mathrm{LSC} \end{cases} \tag{8}$$

where $\{h, j, l\} \in \mathbb{Z}$. This effect is referred to as intermodulation distortion and stems from the inherent nonlinearity in CB-PWM, leading to a double convolution of the PWM sidebands in the frequency domain when modulation signal is of multiple frequencies (here, LF and MF). Consequently, it results in a combination

of sideband harmonics around integer multiples of the equivalent carrier frequency [27], [28]. The impact of these sideband harmonics on the grid current total harmonic distortion (THD) is more severe at lower values of $m_{f,\mathrm{MF}}$. Take, for instance, LSC-PWM; the sideband harmonics at the left side of the equivalent carrier frequency $m_{f,\mathrm{LF}} \pm (2j+1)\frac{m_{f,\mathrm{LF}}}{m_{f,\mathrm{MF}}} \pm (2l+1)$ can encroach into the LF range, consequently elevating the grid current THD. Increasing $m_{f,\mathrm{MF}}$, which can be achieved by either increasing $f_{\mathrm{c,eq}}$ or decreasing f_{MF}, reduces these distortions. However, the former approach leads to significant switching losses, while the latter negates the size reduction benefit of the MMC system.In contrast, the proposed modulation method eliminates the modulation of m^*_{MF} by $f_{\mathrm{c,eq}}$ and use a linear sum function to derive n^*, thereby removing the intermodulation effect. Accordingly, the term $(2j+1)\frac{m_{f,\mathrm{LF}}}{m_{f,\mathrm{MF}}}$ is excluded from (8), and the intermodulation sideband harmonics are absent in the grid-side voltage of the arm as can be seen Fig. 9(a).

A similar observation applies to the MF voltage component of the arm. Fig. 9(b) illustrates that the harmonic spectra of the reference and synthesized voltage waveforms deviate around $f_{\mathrm{c,eq}}$ for both PSC and LSC methods. The performance of the PSC method deteriorates further due to the staircase behavior (see Section III-A1). The proposed modulation method eliminates the intermodulation sideband harmonics from v_{y}^{Σ}. This results in a significantly better match with the harmonic spectra of the reference signal compared to conventional methods, as shown in Fig. 9(b). The only considerable harmonic component seen in the harmonic spectra of FD-PWM is $m_{f,\mathrm{MF}}$. To avoid significant distortions in the MF current waveform, the minimum value of the frequency modulation ratio can be estimated by

$$m_{f,\mathrm{MF}} \geq \frac{4}{\delta\tilde{i}_p N} \tag{9}$$

where $\delta\tilde{i}_p$ denotes the allowable maximum relative peak-to-peak ripple of the MF current. The mathematical derivation of (9) is provided in Appendix.

IV. Soft Switching Operation of the MMC

The soft-switching operation of both the LVC and the MMC (partially) can be achieved by selecting appropriate circuit parameters. Fig. 10 shows the typical voltage and current waveforms of the MMC arm and the LVC. As can been seen, the arm voltage and current are composed of an LF (differential-mode) component and an MF (common-mode) component. Considering the DAB operation, the switching events that synthesize v_{S} (in the LVC) and $2v_0^{\Sigma}$ (in the MMC) can all be zero-voltage switched. To this end, the current through the MMC's arm and the LVC must fulfill the minimum required commutation value I_{ZVS} at the switching instants. Adjusting the transformer turn ratio n_{tr} allows a unity voltage gain across the isolation stage and therefore a trapezoidal current through the LVC. Considering the fact that DAB converter features ZVS operation throughout the load range when the voltage gain is unity, the LVC can always benefit from ZVS [21]. On the other hand, the MMC's arm current is the aggregate of a sinusoidal current (LF component) and a trapezoidal current (MF component). As a result, ZVS operation of power devices in the MMC depends on the values of the arm current ($I^{\mathrm{x}}_{\mathrm{y-sw}\uparrow}$ and $I^{\mathrm{x}}_{\mathrm{y-sw}\downarrow}$) at the rising and falling edges of the MF component of the arm voltage. Defining the peak value of the LF and MF component of the arm as $\hat{I}^{\mathrm{x}}_{\mathrm{y-LF}}$ and $\hat{I}^{\mathrm{x}}_{\mathrm{y-MF}}$, the respective maximum and minimum switching currents during the rising and falling edges of the MF component are

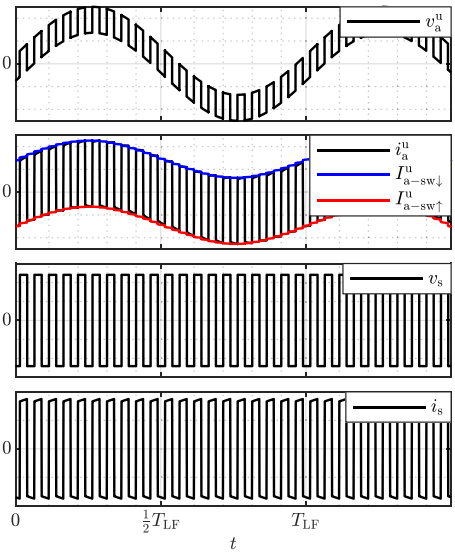

Fig. 10. Ideal current and voltage waveforms of the MMC arm and the LVC.

$$\max\left(\mathrm{I}^{\mathrm{x}}_{\mathrm{y-sw}\uparrow}\right) = \hat{I}^{\mathrm{x}}_{\mathrm{y-LF}} - \hat{I}^{\mathrm{x}}_{\mathrm{y-MF}} \tag{10}$$

$$\min\left(\mathrm{I}^{\mathrm{x}}_{\mathrm{y-sw}\downarrow}\right) = -\hat{I}^{\mathrm{x}}_{\mathrm{y-LF}} + \hat{I}^{\mathrm{x}}_{\mathrm{y-MF}}. \tag{11}$$

Assuming unity power factor for the grid current and constant instantaneous power for the transformer side, the peak values of the LF and MF components of the arm current are approximated by

$$\hat{I}^{\mathrm{x}}_{\mathrm{y-LF}} = \frac{1}{2}\hat{I}_{\mathrm{y}} = \frac{P}{3\hat{V}_{\mathrm{gy}}} \tag{12}$$

$$\hat{I}^{\mathrm{x}}_{\mathrm{y-MF}} = \frac{1}{3}\hat{I}_{\mathrm{p}} = \frac{P}{3n_{\mathrm{tr}}V_{\mathrm{dc}}}. \tag{13}$$

To achieve ZVS in the MMC, the following conditions must be satisfied:

$$\max\left(\mathrm{I}^{\mathrm{x}}_{\mathrm{y-sw}\uparrow}\right) < -I_{\mathrm{ZVS}} \tag{14}$$

$$\min\left(\mathrm{I}^{\mathrm{x}}_{\mathrm{y-sw}\downarrow}\right) > I_{\mathrm{ZVS}}. \tag{15}$$

Substituting (12) and (13) into (10) and (11) and then rewriting (14) and (15) yields

$$\frac{P}{3n_{\mathrm{tr}}V_{\mathrm{dc}}} - \frac{P}{3\hat{V}_{\mathrm{gy}}} > I_{\mathrm{ZVS}}. \tag{16}$$

As a result, the maximum turn ratio of the transformer to ensure ZVS operation in the MMC is given by

$$n_{\mathrm{tr}} < \frac{\frac{P}{3V_{\mathrm{dc}}}}{I_{\mathrm{ZVS}} + \frac{P}{3\hat{V}_{\mathrm{gy}}}}. \tag{17}$$

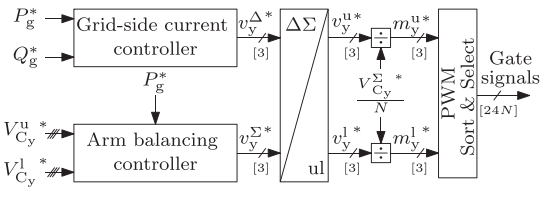

Fig. 11. General control scheme of the MMC.

V. Control of the MMC

A. General Control Approach

For the MMC to function in a stable manner and to track the capacitor voltage and current references, it is crucial to implement an appropriate control strategy for its terminal variables. The mismatch between the average power of the input and output ports of the MMC should be controlled to the power losses of the MMC, otherwise it will disturb the total energy balance within the MMC [16]. As a result, the implementation of the MMC requires a control algorithm to regulate the input and output terminal powers, thereby ensuring the total energy balance within the MMC, as shown in Fig. 11. In this context, $W_{\mathrm{C_y}}^{\Sigma}$ represents the total energy stored in the submodule capacitors of MMC leg y, while $W_{\mathrm{C_y}}^{\Delta}$ is the energy discrepancy between the upper arm and its corresponding lower arm. These variables are expressed as follows:

$$W_{\mathrm{C_y}}^{\Sigma} = \frac{\frac{1}{2}C_{\mathrm{eq,y}}\left(V_{\mathrm{C_y}}^{\mathrm{u}}\right)^2 + \frac{1}{2}C_{\mathrm{eq,y}}\left(V_{\mathrm{C_y}}^{\mathrm{l}}\right)^2}{2} \tag{18}$$

$$W_{\mathrm{C_y}}^{\Delta} = \frac{\frac{1}{2}C_{\mathrm{eq,y}}\left(V_{\mathrm{C_y}}^{\mathrm{u}}\right)^2 - \frac{1}{2}C_{\mathrm{eq,y}}\left(V_{\mathrm{C_y}}^{\mathrm{l}}\right)^2}{2} \tag{19}$$

where $V_{\mathrm{C_y}}^{\mathrm{u}}$ and $V_{\mathrm{C_y}}^{\mathrm{l}}$ are the sum of the submodule capacitor voltages in the upper and its corresponding lower arm, respectively. Here, $C_{\mathrm{eq,y}} = C_{\mathrm{sm}}N$ represent the equivalent capacitance of the arm. The grid-side current controller regulates the active and reactive power exchanged with the grid, and the arm balancing controller ensures total energy balance, as well as an equal energy distribution among the MMC arms. Here, circulating currents between legs are intentionally generated to exchange energy between arms and legs and reach an equal distribution of energy across all of them. The circulating currents are generated as common-mode components, since the grid-side terminal variables (differential-mode components) must track the grid-current reference. To this end, the common-mode voltage of the arm can be expressed as

$$v_{\mathrm{y}}^{\Sigma} = v_0^{\Sigma} + v_{\odot_{\mathrm{y}}}^{\Sigma} \tag{20}$$

where v_0^{Σ} regulates the total energy of the MMC and, therefore, is the same for all three legs. The circulating voltage component $v_{\odot_{\mathrm{y}}}^{\Sigma}$, however, is supposed to regulate the energy difference between the arms by generating circulating currents. Hence, its value may differ among the three legs [16]. The voltage $v_{\odot_{\mathrm{y}}}^{\Sigma}$ is composed of an LF component and an MF component as follows:

$$v_{\odot_{\mathrm{y}}}^{\Sigma} = \overbrace{v_{\odot,1_{\mathrm{y}}}^{\Sigma}}^{\mathrm{LF}} + \overbrace{v_{\odot,2_{\mathrm{y}}}^{\Sigma}}^{\mathrm{MF}}. \tag{21}$$

The total energy mismatch between the legs can be controlled by adjusting $v_{\odot,2_{\mathrm{y}}}^{\Sigma}$, and the energy mismatch between the upper and lower arms can be corrected using $v_{\odot,1_{\mathrm{y}}}^{\Sigma}$. Therefore, v_0^{Σ}, $v_{\odot,1_{\mathrm{y}}}^{\Sigma}$, and $v_{\odot,2_{\mathrm{y}}}^{\Sigma}$ are the three variables that are adjusted by the arm balancing controller. Under balanced circuit parameters, the circulating terms are zero in steady-sate and are not present in the arm common-mode voltage v_{y}^{Σ}. The comprehensive explanation of the circulating components is provided in [8].

It is noteworthy that the grid-side current controller is similar to that of grid-connected voltage source converters. Owing to the decoupling into differential and common mode components, the integration of the proposed method does not influence this controller. Therefore, it will not be studied here, and a detailed discussion can be found in [9].

Fig. 12 illustrates the integration of the proposed method in the control scheme of the MMC. Here, both common-mode $V_{\mathrm{C_y}}^{\mathrm{u}}$ and differential-mode $V_{\mathrm{C_y}}^{\mathrm{l}}$ capacitor voltages are derived from measured electrical variables. These voltages are then converted into equivalent energy representations, $W_{\mathrm{C_y}}^{\Sigma}$ and $W_{\mathrm{C_y}}^{\Delta}$, using (18) and (19) to linearize the feedback loop.

The differential-mode arm energy, $W_{\mathrm{C_y}}^{\Delta}$, is compared to its nominal reference, typically zero, signifying no desired energy disparity between the arms in different legs of the MMC. Any deviation from this reference is processed by a proportional–integral (PI) controller, generating a corresponding power correction term. This term is then scaled by the normalized grid voltage, $\frac{v_{\mathrm{gy}}}{\hat{V}_{\mathrm{g}}}$, to generate the setpoint for $v_{\odot,1_{\mathrm{y}}}^{\Sigma^*}$, regulating the energy balancing between the arms in all MMC's legs.

Concurrently, the common-mode energy for each phase, $W_{\mathrm{C_y}}^{\Sigma}$, is averaged across all three phases to produce $W_{\mathrm{C_0}}^{\Sigma}$, representing the mean energy level in the MMC's arms. This mean value is then compared to the reference of common-mode energy stored in phase y, $W_{\mathrm{C_y}}^{\Sigma^*}$ (the same value for $\mathrm{y} \in \{\mathrm{a}, \mathrm{b}, \mathrm{c}\}$). The discrepancy is fed to the second PI controller that computes an additional power error $\Delta P_{\mathrm{MF_0}}$, to regulate the total energy stored in the MMC capacitors. The third PI controller ensures the common-mode capacitor energy $W_{\mathrm{C_y}}^{\Sigma}$ of the MMC legs matches to the mean value $W_{\mathrm{C_0}}^{\Sigma}$, thereby balancing the energy distribution between the MMC legs.

For prompt control action, the grid power reference, P_{g}^*, is added as a feedforward element to the PI controller's output. This addition yields the MF power reference, $P_{\mathrm{MF_0}}^*$, which is applied uniformly to all MMC legs. The calculated power error $\Delta P_{\mathrm{MF_y}}$ is added to $P_{\mathrm{MF_0}}^*$ to adjust the power reference for each individual leg, thereby ensuring an energy balance between the the arms in each MMC leg.

B. Integration of FD-PWM and Soft Switching Operation

To achieve effective integration of FD-PWM and soft switching, the control scheme of the ac/ac MMC must be adapted to generate precise phase and amplitude references for the MF

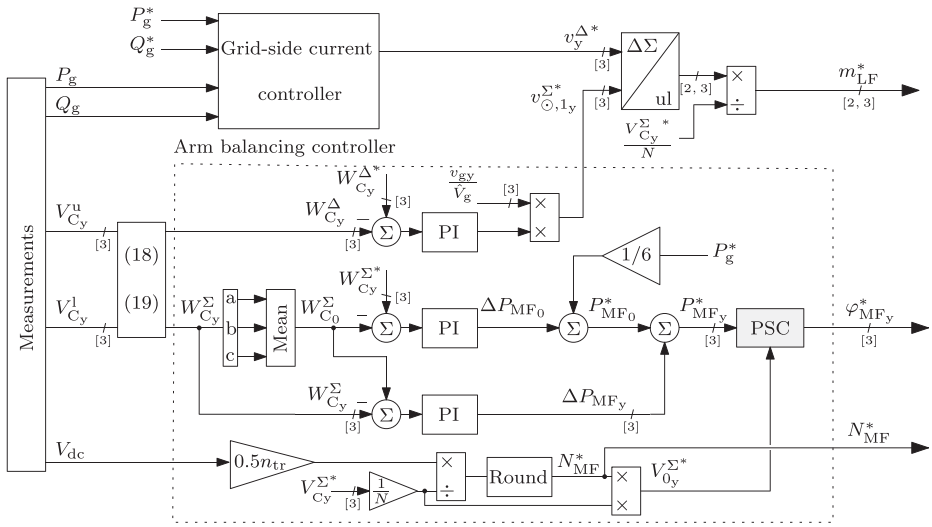

Fig. 12. Integration of the proposed method in the control scheme of the MMC.

component of the arm voltage. First, the MF power reference, $P^*_{\mathrm{MF_y}}$, must be converted into corresponding phase-shift angle references, denoted as $\varphi^*_{\mathrm{MF_y}}$. As expressed in (2), the magnitude of the MF voltage component V_0^{Σ} for each arm is required for the computation of these phase angle references. To minimize the power losses in the DAB-like operation, it is imperative that the voltage gain across the isolation transformer is equal to the transformer turn ratio [21]. This necessitates that the amplitude of the MF component of each arm, $V_0^{\Sigma^*}$, closely approximates the half of output dc voltage as referred to the primary side of the transformer. Achieving this, the half of the primary-referred output voltage is divided by the nominal submodule voltage, and the result is then fed to a round function. This operation yields the discrete count N^*_{MF} of submodules that should be actively switching to synthesize the desired MF voltage component as follows:

$$N^*_{\mathrm{MF}} = \left\lfloor \frac{0.5 n_{\mathrm{tr}} V_{\mathrm{dc}} N}{V_{\mathrm{Cy}}^{\Sigma^*}} \right\rceil . \tag{22}$$

Using the MF component amplitude information, $\varphi^*_{\mathrm{MF_y}}$ can be calculated for all the phases and. The MF components $v_0^{\Sigma^*}$ and $v_{\odot,2_{\mathrm{y}}}^{\Sigma^*}$ of the arm can be constructed by FD-PWM [see Fig. 8(a)] using $\varphi^*_{\mathrm{MF_y}}$ and N^*_{MF}.

VI. Simulation Results

The converter is modeled and simulated in PLECS with the circuit parameters given in Table II. The circuit design parameters are chosen based on Appendix and (2) and (24)–(25). The simulated converter uses an averaged model to represent the MMC arms [9]. This is a fast simulation model that does not take into account the PWM modulator and switching events. However, given that the bandwidths of the PI controllers are much lower than the switching harmonics, the switching-ripple-free waveforms of the converter and the stability of the controllers can be studied through the averaged model [16].

TABLE II
Simulated Circuit Parameters

	Parameter	Value
Grid		
Grid line–line voltage	$\sqrt{3}V_{\mathrm{g}}$	25 kV
Grid frequency	f_{g}	50 Hz
Line inductance	L_{g}	8 mH
MMC		
Equivalent capacitance of the arm	C_{eq}	55 µF
Arm inductance	L_{arm}	750 µH
Number of submodules per arm	N	31
Derated blocking voltage of power devices	V_{b}	1 kV
MFT		
Turn ratio	n_{tr}	15
Leakage inductance	L_{l}	100 µH
LVC		
Output dc voltage	V_{dc}	800 V
Switching frequency	f_{MF}	10 kHz

A. Results

Fig. 13 shows the converter's key waveforms in the case of a power step from 1 to 0.5 MW. The grid-side current is balanced and responds promptly to the modified power setpoint, as expected. The transient power change induces a temporary deviation in the arm capacitor voltages. However, the arm balancing controller effectively mitigates this imbalance by redistributing the energy difference between the arms. Consequently, all capacitor voltages converge to the same value within a few grid cycles. It is noteworthy that this energy balancing relies on circulating currents during the transient state. Once balance is achieved, no circulating current is generated by the controller.

Maintaining balanced volt–seconds across the magnetic components is crucial, as deviations can lead to dc-bias currents and compromise the performance of arm inductors and the MFT. To address this challenge and prevent dc-bias currents upon a change in the power setpoint, a dynamic phase-shift update strategy is implemented, as detailed in [29]. As can be seen in

TABLE III
EXPERIMENTAL PARAMETERS

	Symbol	Value
Grid		
Grid line–line voltage	$\sqrt{3}V_{\mathrm{g}}$	380 V
Grid frequency	f_{g}	50 Hz
MMC		
Number of submodules per arm	N	4
Submodule dc-link capacitance	C_{sm}	5 mF
Arm inductance	L_{arm}	2.3 mH
Carrier frequency	f_{c}	20 kHz
MFT		
Turn ratio	n_{tr}	1
Leakage inductance	L_l	20 µH
Magnetizing inductance	L_m	17 mH
LVC		
Output dc voltage	V_{dc}	250 V
Switching frequency	f_{MF}	8, 10 kHz

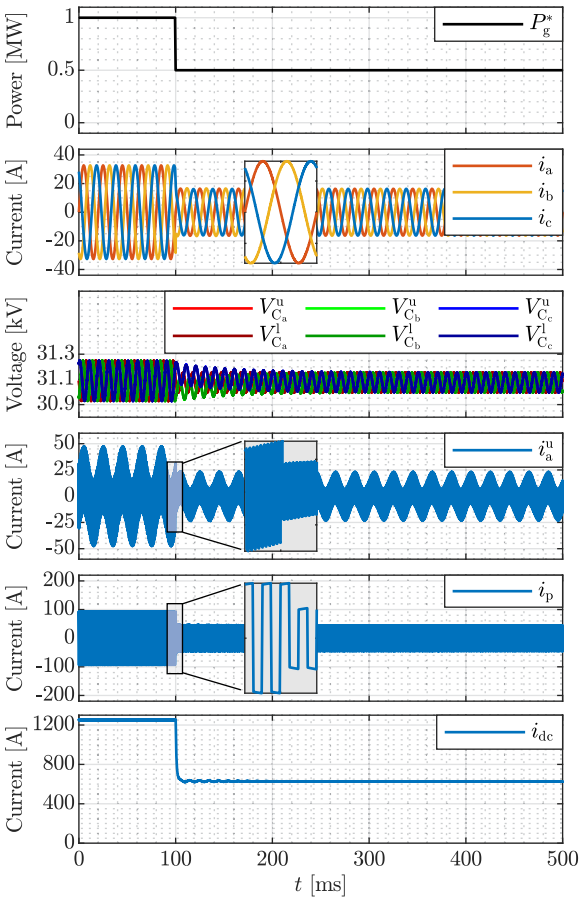

Fig. 13. Simulation results for a step change in the power reference P_{g}^{*} from 1 to 0.5 MW.

Fig. 13, the step change in power does not introduce any dc component in the current.

The arm current of phase a is plotted in Fig. 13. Due to the balanced nature of the grid voltage and current and the balancing controller, the currents of the other phases are similar. As can be seen, the arm current always satisfies the constraints derived in (14) and (15). Using the dynamic phase-shift update method,

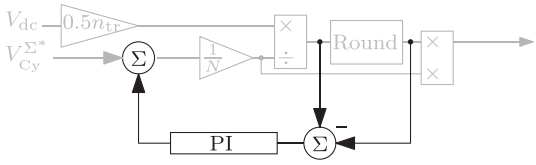

Fig. 14. Outer control loop to adjust the capacitor voltage reference.

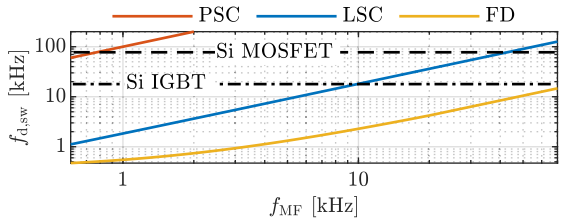

Fig. 15. Scaling of the average switching frequency per device of the MMC in terms of the operating frequency of the transformer for different modulation methods with $\delta\tilde{i}_p = 12.5\%$ and $f_{\mathrm{c,eq}} \geq 20$ kHz. The theoretical power-frequency capability of power devices are derived from [31].

these constraints are met even during the power setpoint change, as can be seen in the zoomed graph in Fig. 13. As a result, all the switching events in the MMC that are associated with the MF component are zero-voltage switched. Since, there is only MF current through the LVC, its power switches can always achieve ZVS operation.

B. Discussion

1) Optimized MF Current Shape: The analysis of the MFT current i_{p} reveals a trapezoidal waveform without flat tops. This deviation from the ideal waveform arises due to the inherent limitation of the MMC in generating the exact primary-referred secondary voltage with its discrete voltage levels. To improve the waveform quality, an outer control loop can be implemented (as depicted in Fig. 14). This loop dynamically adjusts the MMC capacitor voltage setpoint to ensure the half of the primary-referred secondary voltage is an integer coefficient of the submodule capacitor voltage. This, in turn, leads to a more accurate reproduction of the ideal waveform in the MFT current. It is important to note that this outer control loop can be designed to have a much lower bandwidth compared to the other control loops within the battery charger system. This is because the dynamics of voltage change in a battery charging application are inherently slow. The outer loop will not introduce significant delays or negatively impact the performance of the faster inner control loops.

2) Scaling of the Switching Frequency: Applying the constraints detailed in Section III and the design circuit parameters listed in Table II, the scaling law of the average switching frequency per device $f_{\mathrm{d,sw}}$ is illustrated in Fig. 15. In the figure, three modulation methods—PSC, LSC, and FD—are compared against the theoretical power-frequency capabilities of Si IGBT and Si MOSFET power devices. As shown, the proposed modulation method (FD-PWM) exhibits a significantly slower increase in the average switching frequency with respect to the operating

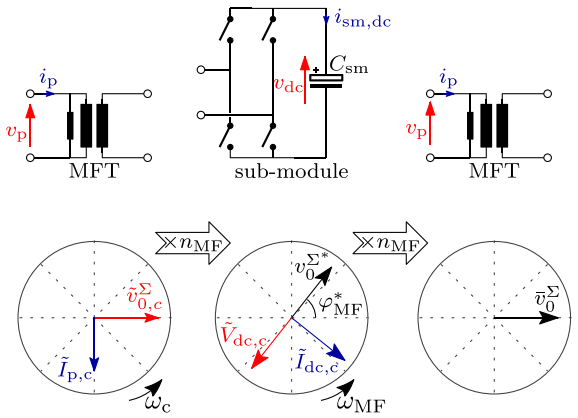

Fig. 16. Resulting voltage and current ripples in the transformer and arm currents, as well as the submodule DC-link variables, under assumption that $m_{f,\mathrm{MF}} = 2$.

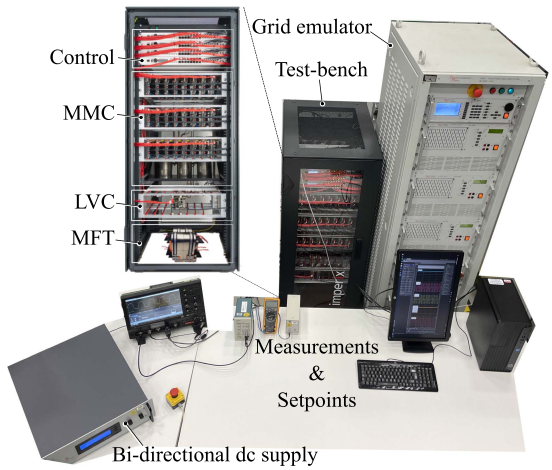

Fig. 17. Test-bench of the MMC-based charger [8].

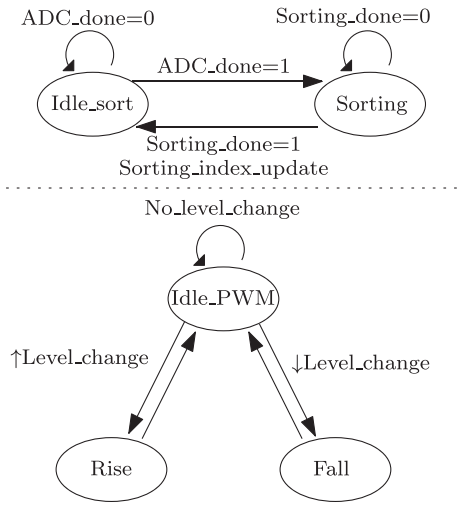

Fig. 18. State machines of the implemented sort and select and PWM generation.

frequency of the transformer f_{MF} compared to the conventional methods (PSC and LSC). This slower growth in the switching frequency allows for the use of cost-effective designs based on Si IGBT or Si MOSFET devices, even as the operating frequency of the MFT increases.

3) Right Selection of the Carrier Frequency: In real-world applications, nonidealities that are not accounted for in the averaged model can present challenges. As illustrated in Fig. 9(b), for the proposed modulation method, the largest harmonic component in the spectra of the common-mode voltage of the arm is the carrier-related $m_{f,\mathrm{MF}}$ harmonic ($\tilde{v}^{\Sigma}_{0,c}$). This voltage harmonic generates a ripple current $\tilde{i}_{\mathrm{p,c}}$ through the primary winding of the transformer and the MMC arms, which lags the voltage ripple by 90° and has a frequency of f_{c}. This current ripple is then multiplied by the MF insertion index n^*_{MF}, resulting in a current ripple $\tilde{i}_{\mathrm{dc,c}}$ and, in turn, a voltage ripple $\tilde{v}_{\mathrm{dc,c}}$ both with a frequency of $f_{\mathrm{c}} - (2h+1)f_{\mathrm{MF}}$ in the dc-link of the submodules [30]. Fig. 16 depicts the resulting voltage and current ripples in the transformer and arm currents, as well as the submodule dc-link variables. As can be seen in Fig. 16, for the voltage ripple component in the submodule dc-link to generate a nonzero average voltage $\bar{v}^{\Sigma}_0$ in the submodule ac-link and therefore across the transformer winding, it should share the same frequency with the MF insertion index f_{MF}. This can be avoided through adequate selection of the ratio between the carrier frequency and the operating frequency of the transformer as follows:

$$f_{\mathrm{c}} \neq (2h+2)f_{\mathrm{MF}} \Rightarrow m_{f,\mathrm{MF}} \neq (2h+2). \tag{23}$$

If this is not taken into account, dc-bias currents appear through the primary winding of the MFT and the arm inductors, which can deteriorate their function and the overall performance of the converter.

VII. Experimental Verification

Experimental results are obtained from an MMC-based ac/dc test-bench which is shown in Fig. 17 . The test-bench comprises three main components: an MMC, an MFT, and a full-bridge ac/dc converter. The MMC consists of 24 submodules, with each arm consisting of four submodules (IMPERIX PEH2015). These submodules are implemented as full-bridge converters utilizing IGBT switches. The MFT is constructed using Metglas AMCC (2605SA1) series cut cores. Furthermore, the ac/dc converter is realized as a full-bridge converter using two half bridges (IMPERIX PEB8038), which employ SiC MOSFETs. The circuit parameters of the scaled-down prototype, which differ from the simulation parameters for the real-scale system, are given in Table III.

The implementation of a sort and select algorithm for MMC on an FPGA is shown in Fig. 18. The algorithm is designed to precisely control the switching states of the MMC submodules to achieve the desired insertion index (output voltage level) while minimizing the number of switching events. Our approach utilizes a dual-state machine setup: one that handles the sorting of capacitor voltages and another that manages the generation of PWM signals. The sorting process begins when an ADC completion pulse is received and ends with generating the sorting index for the capacitor voltages. Simultaneously, a separate state machine adjusts the physical PWM outputs to each submodule

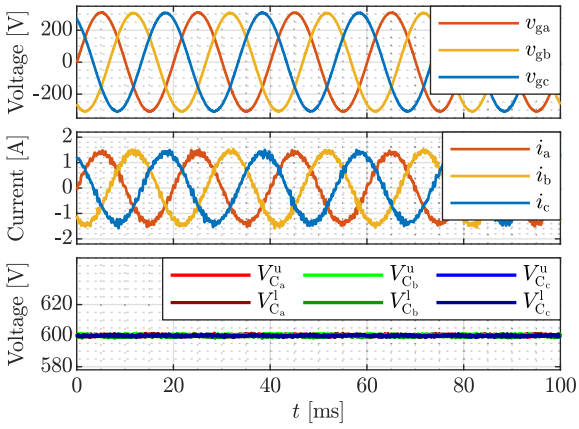

Fig. 19. Measured LF-terminal waveforms and sum of the submodule capacitor voltages of the arm. A 5th-order Bessel low-pass filter with a cutoff frequency of 10 kHz is employed as an antialiasing filter for grid current measurements.

based one the requested level change, sorted voltages, and the polarity of the arm current. In case the generated voltage level matches the required insertion index, no submodule will switch. As a result, the number of switching events can be minimized [32]. This feature is also critical for the proposed method, since it guarantees that there is no rising or falling switching event when a decrease or increase in the voltage level is requested, respectively.

Fig. 19 depicts the LF-terminal waveforms of the MMC and summed capacitor voltages of the arms for a power flow of $P_{\mathrm{g}}^{*} = 650\,\mathrm{W}$ and $f_{\mathrm{MF}} = 8\,\mathrm{kHz}$. The prototype is primarily designed for the MF ranging from 0–1 kHz. As a result, the arm inductance is quite high, reducing the maximum power that can be transferred at elevated frequencies, limiting it to 650 W. As depicted in Fig. 19, the average capacitor voltage of the submodules remains stable at the setpoint value of $V_{\mathrm{C}}^{\Sigma *} = 600\,\mathrm{V}$.

Fig. 20 shows the arm voltage and current waveforms of the MMC. It also shows a zoom of the same plot in the highlighted time interval in Fig. 20(a), that is the worst case scenario for soft-switching operation. As can be seen, at the rising edge of the MF component of the arm, the arm current is negative, and the absolute value is large enough to have ZVS turn-ON of power switches ($I_{\mathrm{ZVS}} = 0.1\,\mathrm{A}$).

The measured MF terminal waveforms are illustrated in Fig. 21. As can be seen, the switching current at both the rising and falling edges of the secondary voltage is sufficiently large to ensure ZVS turn-ON of the power devices in the LVC ($I_{\mathrm{ZVS}} = 0.4\,\mathrm{A}$). The current ripple observed in the transformer's primary current is attributed to the carrier frequency of 20 kHz.

Since $m_{f,\mathrm{MF}} = 2.5$ was selected according to (23), no dc-bias current is present in the transformer winding current. To illustrate the effects of an incorrect selection, f_{MF} was set to 10 kHz ($m_{f,\mathrm{MF}} = 2$), with the resulting waveforms depicted in Fig. 22. As observed, the transformer winding current exhibits a bias of 110 mA due to the nonzero average voltage applied by the MMC's arms, highlighting the importance of correctly choosing $m_{f,\mathrm{MF}}$. To avoid this, the carrier frequency can also be altered according to (23).

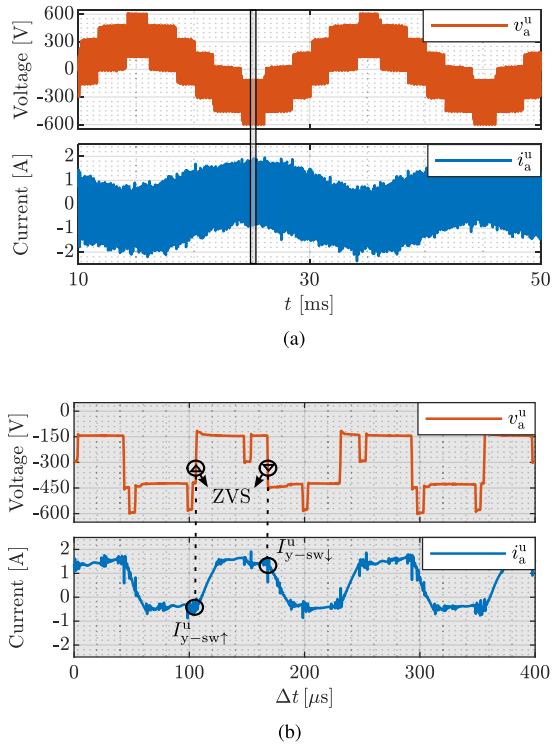

Fig. 20. Measured arm variables for the power flow of $P_{\mathrm{g}}^{*} = 650\,\mathrm{W}$. (a) Overview of the arm voltage and current waveforms. (b) Same results in the zoomed time interval.

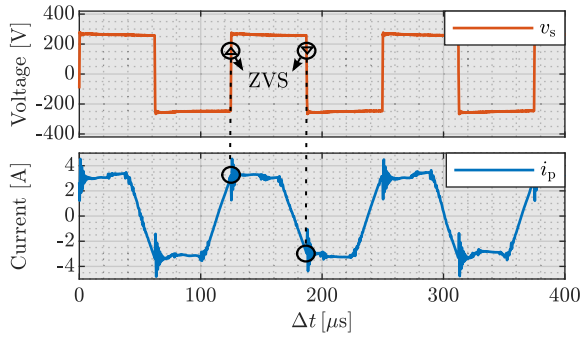

Fig. 21. Measured ac-link waveforms of the LVC for the power flow of $P_{\mathrm{g}}^{*} = 650\,\mathrm{W}$ and the MF of $f_{\mathrm{MF}} = 8\,\mathrm{kHz}$.

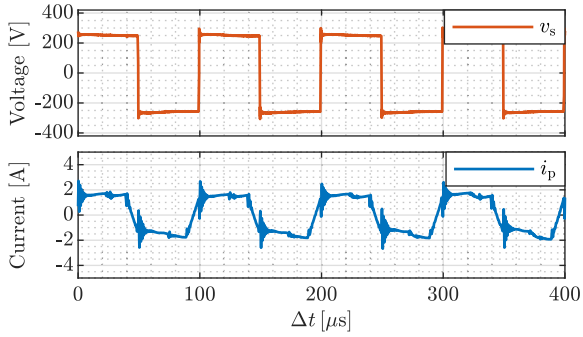

Fig. 22. Measured ac-link waveforms of the LVC for the MF of $f_{\mathrm{MF}} = 10\,\mathrm{kHz}$.

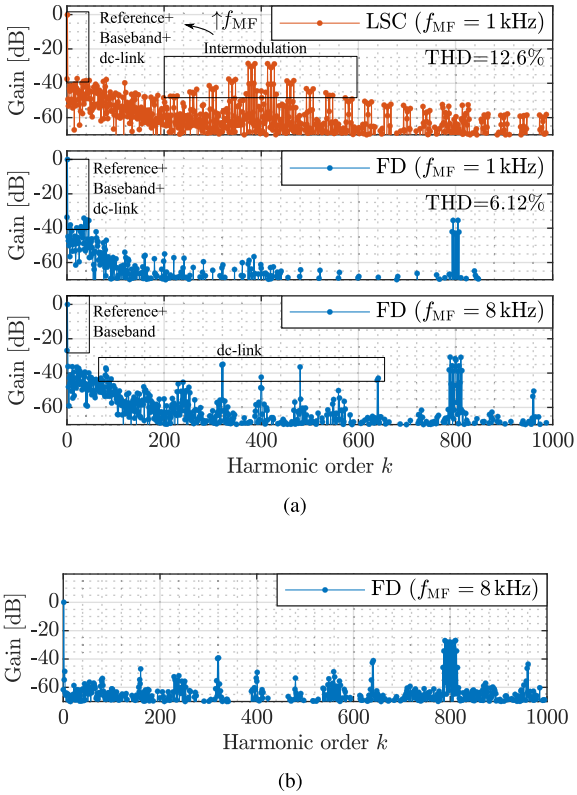

Fig. 23. Harmonic performance comparisons (the values are normalized based on the fundamental component $f_g = 50$ Hz). (a) Harmonic spectra of the measured grid current i_a of LSC-PWM for and FD-PWM methods. (b) Harmonic spectra of the measured differential-mode arm voltage v_a^{Δ} for the FD-PWM method.

Fig. 23(a) presents the harmonic spectra of the grid current for both LSC-PWM and the proposed modulation method. To ensure a fair comparison, and considering the limited time resolution of LSC-PWM, the MF is first set to $f_{MF} = 1$ kHz for both methods. As illustrated, the harmonic spectra of the proposed method are free of the intermodulation sideband harmonics that are prominently visible around the carrier frequency $f_c = 20$ kHz in LSC-PWM, which reduces the THD, as shown in Fig. 23(a). Supposedly, if the operating frequency of the transformer f_{MF} increases, these sideband harmonics shift toward LF range with even higher amplitudes. Due to the FD operation of the proposed method, the intermodulation harmonics are not present using FD-PWM. In addition, there are significant harmonic components at lower frequencies. These large harmonic components around the operating frequency of the transformer are expected due to the voltage ripple present in the dc-link of the submodules. The harmonic components of the voltage ripple are modulated by the insertion index of the arm n and manifest in the arm voltage. It should be noted that the resulting harmonic content and THD values are intended for a relative comparison of the modulation strategies and may not comply with the grid code due to the low number of submodules and the low power level of the test-bench.

The bottom graph of Fig. 23(a) illustrates the harmonic spectra of the grid current when the transformer operates at 8 kHz. This measurement is conducted only for FD-PWM, as the limited time resolution of LSC-PWM does not allow the stable operation of the MMC at this frequency range. Increasing f_{MF} from 1 to 8 kHz raised the average switching frequency per device in the MMC from 2.7–4.5 kHz. However, the average switching frequency scales almost linearly with the operating frequency of the transformer using the LSC-PWM method. It is evident that harmonic components around the transformer's operating frequency (e.g., 8 kHz) are attenuated more by the arm inductance. However, higher order harmonics (e.g., 16, 20, 24 kHz) experience less attenuation. This is primarily because these high-frequency harmonics originate from LF harmonics in the submodule's dc-link (see Section VI-B3), which are modulated back by the submodules and appear as high-frequency harmonics in the arm voltage. Consequently, their amplitude is larger due to their origin from LF harmonics in the dc-link voltage. These higher order harmonics can be significantly reduced by increasing the number of submodules N and minimizing the ripple current. Therefore, for a full-scale ac/ac MMC, these harmonics can be neglected.

In addition to the dc-link related harmonics, other LF harmonics are still present in the grid current spectra. To further investigate this, the upper arm and lower arm voltages were measured, and the differential-mode component was derived by subtracting them. The harmonic spectra of this voltage component are shown in Fig. 23(b). It is evident that most of the LF harmonics seen in the current spectra are not present here, suggesting that a background noise or nonidealities in the converter circuit are the main cause this part of the LF distortions and they are not due to the modulation method itself.

VIII. Conclusion

This article presents an FD modulation strategy and a soft-switching technique for the ac/ac MMC with rectangular-wave output, aiming to achieve a higher operating frequency for the isolation stage. The core concept of the proposed modulation method involves separating the LF and MF components within the MMC arm's modulator and selecting different modulator types for each. This separation offers two key benefits: first, it facilitates higher time resolution for generating the MF voltage component, leading to improved waveform synthesis; and second, it eliminates intermodulation sideband harmonics in the generated arm voltage, resulting in better harmonic performance. Furthermore, the proposed method leverages a DAB-like operation to achieve ZVS for all the switching events in the LVC and those associated with the MF component in the MMC, given the correct selection of the MFT's turn ratio.

A dedicated control scheme is developed to address the capacitor voltage balancing of the MMC, the FD modulation strategy, and the soft-switching operation of both the LVC and the MMC. The full-scale MMC-based charger with the developed control scheme is simulated using the arm averaged model. With the proposed modulation strategy, the average switching frequency per device increases more gradually with increasing the MFT's operating frequency compared to conventional modulation methods. This allows for the use of low-cost power devices, such as IGBTs, near the optimal operating frequency of

TABLE IV
DESIGN PARAMETERS OF THE 3PH-1PH MMC

Parameter	Formula
MMC arm max. voltage	$\hat{V}_{\rm gy} + \frac{n_{\rm tr} \cdot V_{\rm dc}}{2}$
MMC arm max. current	$\frac{P}{3\hat{V}_{\rm gy} \cdot {\rm PF}} + \frac{P^2}{3 n_{\rm tr} V_{\rm dc}} \cdot \frac{\pi}{\pi - \varphi}$
Min. number of sub-modules per arm, N	$\left\lceil \frac{\hat{V}_{\rm gy} + \frac{n_{\rm tr} \cdot V_{\rm dc}}{2}}{V_{\rm b}} \right\rceil$
Number of switches	$24N$
Number of MFTs	1

the MFT (7–10 kHz). It is found that specific ratios of the carrier frequency to the MFT's operating frequency must be avoided, as they can lead to a dc voltage component across the primary winding of the MFT.

The practical value of the theoretical findings is demonstrated with a scaled-down MMC-based prototype which interfaces a 250 V dc bus with a three-phase 380 V, 50 Hz ac source. The proposed modulation strategy and developed control scheme are successfully implemented on the prototype, yielding well-balanced capacitor voltages, desired soft-switching operation, and improved harmonic performance.

APPENDIX

Design parameters of the 3ph-1ph MMC are presented in Table IV [9], [24], [33], where PF and $V_{\rm b}$ represent the power factor of the grid current and the derated blocking voltage of the power devices of the submodule, respectively.

The minimum required capacitance for submodules, taking into account the permissible voltage fluctuation on the submodule dc-link $\Delta v_{\rm sm}$, as given by Marca et al. [34] is equal to

$$C_{\rm sm} \geq \frac{V_y^{\Delta} I_y}{N \omega {\rm g} \Delta v_{\rm sm} V_{\rm sm}} \tag{24}$$

where N, $\omega_{\rm g}$, and $V_{\rm sm}$ represent the number of submodules per arm, the angular frequency of the grid voltage, and the submodule dc-link voltage, respectively.

The permissible grid current ripple $\Delta \tilde{i}_y$ leads to a minimum arm inductance

$$\frac{L_{\rm arm}}{2} \geq \frac{T_{\rm m} V_{\rm sm}}{8 \Delta \tilde{i}_y} + L_{\rm g} \tag{25}$$

where $T_{\rm m}$ denotes the period of PWM [35].

The MF current ripple and its peak value [24] are obtained by

$$\begin{cases} \Delta \tilde{i}_{\rm p} = \frac{1}{2L} T_{\rm m} V_{\rm sm} \\ \hat{I}_p = \frac{n_{\rm tr} V_{\rm dc} \varphi}{2\pi f_{\rm MF} L}. \end{cases} \tag{26}$$

Assuming $\varphi = \frac{\pi}{4}$ and $n_{\rm tr} V_{\rm dc} = N V_{\rm sm}$, the relative peak-to-peak ripple of the MF current can be obtained by

$$\delta \tilde{i}_{\rm p} = \frac{\Delta \tilde{i}_{\rm p}}{\hat{I}_{\rm p}} = \frac{\frac{1}{2L} \frac{1}{f_{\rm c}} V_{\rm sm}}{\frac{n_{\rm tr} V_{\rm dc} \varphi}{2\pi f_{\rm MF} L}} = \frac{4}{m_{\rm f,MF} N}. \tag{27}$$

REFERENCES

[1] G. Zheng, Y. Chen, and Y. Kang, "A modular multilevel converter (MMC) based solid-state transformer (SST) topology with simplified energy conversion process and magnetic integration," *IEEE Trans. Ind. Electron.*, vol. 68, no. 9, pp. 7725–7735, Sep. 2021.

[2] H. Tu, H. Feng, S. Srdic, and S. Lukic, "Extreme fast charging of electric vehicles: A technology overview," *IEEE Trans. Transport. Electrific.*, vol. 5, no. 4, pp. 861–878, Dec. 2019.

[3] R. Kopacz, D. Menzi, F. Krismer, J. Rbkowski, J. W. Kolar, and J. Huber, "New single-stage bidirectional three-phase AC-DC solid-state transformer," *Electron. Lett.*, vol. 60, no. 2, 2024, Art. no. e13084. [Online]. Available: https://ietresearch.onlinelibrary.wiley.com/doi/abs/10.1049/ell2.13084

[4] T. Friedli and J. W. Kolar, "Comprehensive comparison of three-phase AC-AC matrix converter and voltage DC-link back-to-back converter systems," in *Proc. Int. Power Electron. Conf. - ECCE Asia*, 2010, pp. 2789–2798.

[5] J. E. Huber, D. Rothmund, and J. W. Kolar, "Comparative evaluation of isolated front end and isolated back end multi-cell SSTs," in *Proc. IEEE 8th Int. Power Electron. Motion Control Conf.*, 2016, pp. 3536–3545.

[6] J. Huber, P. Wallmeier, R. Pieper, F. Schafmeister, and J. W. Kolar, "Comparative evaluation of MVAC-LVDC SST and hybrid transformer concepts for future datacenters," in *Proc. Int. Power Electron. Conf.*, 2022, pp. 2027–2034.

[7] Y. P. Marca, M. G. L. Roes, C. G. E. Wijnands, J. L. Duarte, and H. Huisman, "Single-stage MV-connected charger using an AC/AC modular multilevel converter," *Energies*, vol. 17, no. 12, 2024, Art. no. 2998. [Online]. Available: https://www.mdpi.com/1996-1073/17/12/2998

[8] K. Pouresmaeil, M. G. Roes, N. H. Baars, and C. G. Wijnands, "Switching loss reduction for an MMC-fed AC/DC converter," *IEEE Open J. Power Electron.*, vol. 5, pp. 70–78, 2024.

[9] Y. P. Marca, M. G. L. Roes, J. L. Duarte, and K. G. E. Wijnands, "Isolated MMC-based AC/AC stage for ultrafast chargers," in *Proc. IEEE 30th Int. Symp. Ind. Electron.*, 2021, pp. 1–8.

[10] Y. P. Marca, M. G. L. Roes, J. L. Duarte, and K. Wijnands, "Square wave operation to reduce pulsating power in isolated MMC-based ultrafast chargers," in *Proc. 24th Eur. Conf. Power Electron. Appl.*, 2022, pp. 1–7.

[11] N. Djekanovic and D. Dujic, "Design optimization of a MW-level medium frequency transformer," in *Proc. PCIM Europe 2022; Int. Exhib. Conf. Power Electron., Intell. Motion, Renewable Energy Energy Manage.*, 2022, pp. 1–10.

[12] T. B. Gradinger, R. M. Burkart, and M. Mogorovic, "Influence of operating frequency on high-power medium-voltage medium-frequency transformers," in *Proc. 24th Eur. Conf. Power Electron. Appl.*, 2022, pp. 1–10.

[13] T. Nakanishi and J.-I. Itoh, "Evaluation of control methods for isolated three-phase AC-DC converter using modular multilevel converter topology," in *Proc. IEEE ECCE Asia Downunder*, 2013, pp. 52–58.

[14] M. Glinka and R. Marquardt, "A new AC/AC multilevel converter family," *IEEE Trans. Ind. Electron.*, vol. 52, no. 3, pp. 662–669, Jun. 2005.

[15] S.-i. Hamasaki, K. Takahashi, Y. Fujita, and T. Daido, "New circuit structure applying MMC and its control for quick charger system," in *Proc. Int. Power Electron. Conf.*, 2022, pp. 2364–2369.

[16] S. Milovanović and D. Dujić, "Comprehensive comparison of modular multilevel converter internal energy balancing methods," *IEEE Trans. Power Electron.*, vol. 36, no. 8, pp. 8962–8977, Aug. 2021.

[17] K. Budo and T. Takeshita, "An isolated medium-voltage AC–DC converter using level-shifted PWM control of a modular matrix converter," in *Proc. 22nd Eur. Conf. Power Electron. Appl.*, 2020, pp. P.1–P.10.

[18] R. Mo, H. Li, and Y. Shi, "A phase-shifted square wave modulation (PS-SWM) for modular multilevel converter (MMC) and DC transformer for medium voltage applications," *IEEE Trans. Power Electron.*, vol. 34, no. 7, pp. 6004–6008, Jul. 2019.

[19] M. Vasiladiotis, T. Geyer, and A. Christe, "Modulation of AC/AC MMC," originally assigned to ABB Schweiz AG, U.S. Patent US10554142B2, Feb. 4, 2020. [Online]. Available: https://patents.google.com/patent/US10554142B2

[20] M. Vasiladiotis, A. Christe, T. Geyer, and A. Faulstich, "Decoupled modulation concept for three-to-single-phase direct AC/AC modular multilevel converters for railway interties," in *Proc. 19th Eur. Conf. Power Electron. Appl.*, 2017, pp. P.1–P.9.

[21] R. Haneda and H. Akagi, "Design and performance of the 850-V 100-kW 16-kHz bidirectional isolated DC–DC converter using SiC-MOSFET/SBD H-bridge modules," *IEEE Trans. Power Electron.*, vol. 35, no. 10, pp. 10013–10025, Oct. 2020.

[22] S. Cui, J. Hu, and R. W. De Doncker, "Control and experiment of a TLC-MMC hybrid DC–DC converter for the interconnection of MVDC and HVDC grids," *IEEE Trans. Power Electron.*, vol. 35, no. 3, pp. 2353–2362, Mar. 2020.
[23] F. Dijkhuizen, J. Duarte, and W. van Groningen, "Multi-level converter with auxiliary resonant-commutated pole," in *Proc. Conf. Rec. IEEE Ind. Appl. Conf., 33rd IAS Annu. Meeting*, 1998, pp. 1440–1446, vol. 2.
[24] K. Pouresmaeil, J. Duarte, K. Wijnands, M. Roes, and N. Baars, "Single-phase bidirectional ZVZCS AC-DC converter for MV-connected ultra-fast chargers," in *Proc. PCIM Europe; Int. Exhib. Conf. Power Electron., Intell. Motion, Renewable Energy Energy Manage.*, 2022, pp. 1–7.
[25] M. Guan, Z. Xu, and H. Chen, "Control and modulation strategies for modular multilevel converter based HVDC system," in *Proc. IECON 37th Annu. Conf. IEEE Ind. Electron. Soc.*, 2011, pp. 849–854.
[26] P. Sochor and H. Akagi, "Theoretical and experimental comparison between phase-shifted PWM and level-shifted PWM in a modular multilevel SDBC inverter for utility-scale photovoltaic applications," *IEEE Trans. Ind. Appl.*, vol. 53, no. 5, pp. 4695–4707, Sep./Oct. 2017.
[27] M. Odavic, M. Sumner, P. Zanchetta, and J. C. Clare, "A theoretical analysis of the harmonic content of PWM waveforms for multiple-frequency modulators," *IEEE Trans. Power Electron.*, vol. 25, no. 1, pp. 131–141, Jan. 2010.
[28] H. d. T. Mouton, B. McGrath, D. G. Holmes, and R. H. Wilkinson, "One-dimensional spectral analysis of complex PWM waveforms using superposition," *IEEE Trans. Power Electron.*, vol. 29, no. 12, pp. 6762–6778, Dec. 2014.
[29] M. Stojadinović, E. Kalkounis, F. Jauch, and J. Biela, "Generalized PWM generator with transformer flux balancing for dual active bridge converter," in *Proc. 19th Eur. Conf. Power Electron. Appl.*, 2017, pp. P.1–P.10.
[30] K. Pouresmaeil, M. Roes, N. Baars, and K. Wijnands, "Active DC-bias mitigation method for a single-phase transformer-connected converter through DC-link measurement," in *Proc. IECON- 49th Annu. Conf. IEEE Ind. Electron. Soc.*, 2023, pp. 1–5.
[31] M. Beheshti, "Wide-bandgap semiconductors: Performance and benefits of GaN versus SiC," *Analog Des. J*, vol. 4, pp. 1–6, 2020.
[32] J. Ançay, "Implementation of the imperix SS-PWM for MMC. Imperix knowledge base," Accessed: May 12, 2023. [Online]. Available: https://imperix.com/doc/implementation/ss-pwm-for-mmc
[33] S. Fuchs, S. Beck, and J. Biela, "Single transformer, MMC based MV power electronic traction transformer," in *Proc. 24th Eur. Conf. Power Electron. Appl.*, 2022, pp. 1–11.
[34] Y. P. Marca, M. G. L. Roes, and K. G. E. Wijnands, "Capacitor voltage ripple and capacitance evaluation in a direct three-phase to single-phase AC/AC MMC," in *Proc. 11th Int. Conf. Power Electron. ECCE Asia*, 2023, pp. 2278–2283.
[35] M. Schnarrenberger, "Der modulare multilevel-umrichter ALS dreiphasige spannungsquelle," Ph.D. dissertation, Karlsruher Inst für Technol., Karlsruhe, Germany, 2019.

Kaveh Pouresmaeil (Graduate Student Member, IEEE) received the B.Sc. degree in electrical engineering from the University of Tabriz, Tabriz, Iran, in 2016, and the M.Sc. degree in power electronics from the Sharif University of Technology, Tehran, Iran, in 2018. Since 2021, he has been working toward the Ph.D. degree in high-power converters for charging infrastructure of electrified transportation with the Electromechanics and Power Electronics group, Eindhoven University of Technology, Eindhoven, The Netherlands.

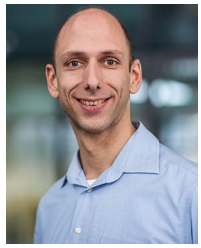

Maurice G. L. Roes (Member, IEEE) received the B.Sc., M.Sc., and Ph.D. degrees from the Eindhoven University of Technology, Eindhoven, The Netherlands, in 2005, 2009, and 2015, respectively, all in electrical engineering.

He was appointed as a Assistant Professor with the Eindhoven University of Technology, in 2016. His research interests include advanced (digital) control of power converters, modern control theory, state estimation, and modeling of multiphysics systems.

Nico H. Baars received the B.Eng. degree from the HAN University of Applied Sciences, Arnhem, The Netherlands, in 2010, and the M.Sc. and Ph.D. (*cum laude*) degrees from the Eindhoven University of Technology, Eindhoven, The Netherlands, in 2013 and 2017, respectively, all in electrical engineering.

After receiving the Ph.D. degree, he started working with Strukton Power, Utrecht, The Netherlands, where he is responsible for power converters for rolling stock and railway power supply applications. Since 2017, he has been a Visiting Researcher with Electromechanics and Power Electronics Group, Eindhoven University of Technology. His research interests include soft-switching and modulation strategies in power converters.

George A. Papafotiou (Member, IEEE) received the diploma and Ph.D. degree in electrical engineering from the Aristotle University of Thessaloniki, Thessaloniki, Greece, in 1997 and 2002, respectively.

In 2021, he joined the Electromechanics and Power Electronics Group, Eindhoven University of Technology, Eindhoven, The Netherlands, where he is currently leading the Power Electronics Lab. From 2017 to 2021, he was Quality and Customer Experience Manager for the System Drives Division of ABB Motion, and from 2012 to 2017 he was responsible for the global R&D activities in control SW and control HW for ABB's MV Drives. From 2006 to 2012, he was with the ABB Corporate Research Center, Dättwil, Switzerland, where he was working on the development of modern control and estimation methods for power electronics applications, and after 2010 leading the Power Electronics Systems Team. From 2003 to 2006, he was with the Automatic Control Laboratory, ETH Zurich, Zurich, Switzerland, where he was working on MPC for hybrid systems, with a special focus on dc–dc converters and induction motor drives.